

Article

Corrosion Behaviors of N80 and 1Cr Tubing Steels in CO₂ Containing Downhole Environment—A Case Study of Underground Gas Storage in LiaoHe Oil Field

Jianfeng Liu ¹, Minghui Li ¹, Mengqi He ¹, Zelin Ma ^{2,*}, Kepei Li ², Ling Wang ¹, Guotao Li ¹, Liguo Zhou ¹, Shaohui Zhang ¹ and Wei Yan ² 

¹ LiaoHe Oilfield Gas Storage Co., Ltd., China National Petroleum Corporation, Panjin 124000, China

² State Key Laboratory of Oil and Gas Resources and Detection, China University of Petroleum, Beijing 102249, China

* Correspondence: 2020216470@student.cup.edu.cn

Abstract: In order to evaluate the effect of chromium content in carbon steel on the corrosion resistance of carbon steel materials, the corrosion behavior of 1Cr and N80 steels was investigated in this study by immersion weight loss method under three different CO₂ partial pressure and temperature conditions in formation water for 72, 168 and 336 h. Detailed material surface morphological characterization was performed by scanning electron microscopy (SEM), energy dispersive spectroscopy (EDS), and confocal laser scanning microscopy (CLSM). The results show that the pitting corrosion of N80 carbon steel is serious at medium temperature and low CO₂ partial pressure (50 °C, 0.30 MPa), and the corrosion rate is significantly higher than that of 1Cr steel. However, at high-temperature and high CO₂ partial pressure (100 °C/0.63 MPa and 114 °C/0.73 MPa), 1Cr steel is more inclined to the mesa corrosion dominated by local corrosion characteristics, and the corrosion rate is seriously higher than that of N80 steel with uniform corrosion. From the experimental results, we can know the corrosion resistance of carbon steel and 1Cr steel is not only affected by the corrosion environment, but also depends on the formation process of the product film, as well as its compactness and integrity characteristics. At low-temperature and low CO₂ partial pressure, 1 wt.% chromium content can provide a certain degree of corrosion resistance, while high temperature and high partial pressure can broaden the application window of carbon steel N80 and weaken the corrosion inhibition effect of chromium.

Keywords: 1Cr steel; carbon steel; CO₂ corrosion; product film; applicable conditions



Citation: Liu, J.; Li, M.; He, M.; Ma, Z.; Li, K.; Wang, L.; Li, G.; Zhou, L.; Zhang, S.; Yan, W. Corrosion Behaviors of N80 and 1Cr Tubing Steels in CO₂ Containing Downhole Environment—A Case Study of Underground Gas Storage in LiaoHe Oil Field. *Coatings* **2023**, *13*, 737. <https://doi.org/10.3390/coatings13040737>

Academic Editor: Peter Rodić

Received: 15 February 2023

Revised: 27 March 2023

Accepted: 28 March 2023

Published: 4 April 2023



Copyright: © 2023 by the authors. Licensee MDPI, Basel, Switzerland. This article is an open access article distributed under the terms and conditions of the Creative Commons Attribution (CC BY) license (<https://creativecommons.org/licenses/by/4.0/>).

1. Introduction

The construction of gas storage is a strategic measure in response to the rapid development of natural gas pipeline networks and the natural gas industry [1]. However, the wellbore string corrosion problem seriously limits the safety of injection and production in gas storage in the early stages of gas storage operation, forming residual drilling fluids, hydrochloric acid, condensate, CO₂, and other complex environments can intensify string corrosion [2–5]. Recently, due to its cost-effectiveness and good corrosion resistance [6–8], low chromium tubing steel with a chromium content of 1 wt.%~5 wt.% has gained attention from researchers as an advanced material for carbon steel and is expected to be an ideal choice for gas storage construction.

1Cr steel and N80 steel are two commonly used materials in the oil and gas industry. Understanding the corrosion behavior of 1Cr steel and N80 steel under different partial pressure and temperature conditions of CO₂ can help in the selection of appropriate materials for oil and gas production applications, and aid in the development of corrosion prevention and mitigation strategies. However, the effectiveness of corrosion resistance

improvement at low chromium content (1 wt.%) still needs to be clarified, and the difference in corrosion resistance between carbon steel and 1Cr alloy steel has yet to be fully studied.

The research on the effective Cr content in low chromium steel has not yet reached a consensus. There are a large number of published studies [7,9–11] that propose that adding 0.5 wt.%~1.0 wt.% Cr can prevent severe mesa corrosion. According to Guo et al. [12], a continuous and ductile inner amorphous layer will cover the entire surface of the specimen, which seems to inhibit localized corrosion when the content of Cr is around 2 wt.%. It has been observed that in an alloy containing 3 wt.% of Cr content, there is competition between the deposition of chromium-containing compounds and FeCO_3 , forming a compact “chromium-rich” FeCO_3 corrosion product film [12–16]. Bai and Chen et al. [17–19] reported that the corrosion product film of N80 steel with 4 wt.% Cr content comprised amorphous Cr_7C_3 , Cr_2O_3 , and FeCO_3 . Ueda and Takabe [20] reported that for 4~5 wt.% chromium steel, the corrosion product film contained a huge amount of chromium content than the matrix after 24 h of immersion and that the samples corroded uniformly without pitting.

Subsequently, the best applicable critical conditions for low-chromium steel are still need to be clarified. Investigations on the corrosion behavior of 1 wt.%, 2 wt.%, 3 wt.%, and 5 wt.% low chromium alloy steels under static conditions of 80 °C and 0.8 MPa CO_2 partial pressure showed slight pitting corrosion on 1Cr steel samples. In contrast, local corrosion was likely to occur on 2Cr steel due to its striped crystal-skinned surface. Both 3Cr and 5Cr steels exhibited uniform corrosion morphology, and 5Cr steel had lower corrosion rates and higher chromium enrichment than 3Cr steel [12,14,16]. Li et al. [21] studied the corrosion behavior of 3Cr and carbon steel under normal temperature and pressure and concluded that local corrosion was likely to occur under these conditions. Numerous studies have examined the effects of temperature on the corrosion behavior of N80 and N80 with 1 wt.% Cr and 4~5 wt.% Cr steel pipes at 78 °C and 1 MPa CO_2 partial pressure [11,18,19,22–27]. Results showed serious and rapid pitting corrosion on N80 pipe samples, while the corrosion rate of the N80 with 1 wt.% was significantly lower. Uniform corrosion was reported for N80 steel with 4~5 wt.% Cr. Sun, Wang, and Wu et al. [28–32] demonstrated that at 60 °C and 1 MPa CO_2 partial pressure, adding 3~5 wt.% Cr eliminated localized corrosion on X65 steel. Li [33] found that at 100 °C and 0.03 MPa CO_2 partial pressure, N80 steel exhibited uniform corrosion with shallow circular pits, 3Cr showed deep pitting corrosion, while a small extent of honeycomb corrosion was noted on 1Cr.

Research on the corrosion mechanism of low chromium steel, especially low alloy steel represented by 1Cr steel, remains to be explored. It is generally assumed that the corrosion resistance of low chromium alloy steel pipes is better than that of ordinary carbon steel in various corrosive environments. However, recent literature has presented conflicting findings, but unfortunately, no deep theoretical exploration has been conducted [13,33]. Therefore, this study aims to uncover the mechanism of CO_2 corrosion behavior of low chromium steel (1Cr) and N80 carbon steel under different conditions to aid in the material selection process for the Shuang-6 gas storage facility at LiaoHe Oilfield, thereby improving safety and reducing economic losses.

2. Materials and Methods

2.1. Material and Style

In this study, we analyzed 1Cr steel and N80 carbon steel samples with the chemical composition shown in Table 1. Each sample was machined into three specimens measuring 25 mm × 10 mm × 3 mm with a 6 mm round hole at one end. Two specimens from each sample were used for weight loss analysis due to corrosion, while the third was used for surface analysis. Before the tests and analysis, the specimens were polished sequentially on the metallographic abrading and polishing machine with 300 #, 600 #, and 1200 # grit silicon carbide abrasive paper. After polishing, the specimens were cleaned with water and degreased with absolute ethanol. The size of the polished specimens was measured with a vernier caliper (accurate to 0.01 mm) and weighed on an analytical

weighing balance (precise to 0.1 mg) before being loaded into the PTFE rack and placed in the high-temperature, high-pressure dynamic reactor.

Table 1. Chemical composition of test samples (% by weight).

Alloy Steel	C	Si	Mn	P	S	Cr	Ni	Mo	V	Cu
N80	0.21	0.24	0.51	0.0024	0.0019	0.03	0.18	0.03	0.01	0.10
1Cr	0.20	0.26	0.41	0.0086	0.0008	1.02	0.10	0.32	0.01	0.01

2.2. Experimental Conditions

The experimental conditions adopted in this study are based on LiaoHe Oil field formation conditions at different vertical depths (Figure 1).

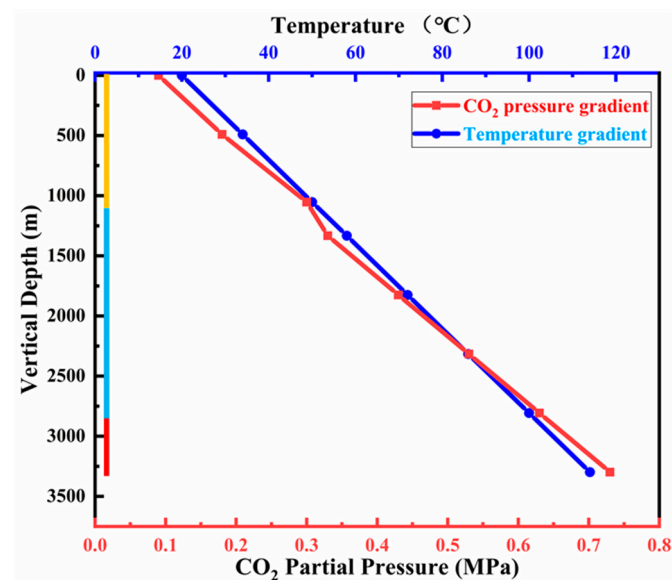


Figure 1. Temperature/partial pressure-well depth profile chart. Note: The meaning of longitudinal axis color division, yellow area represents low temperature formation; the blue area represents the medium temperature stratum; the red area represents high temperature strata.

Based on the above wellbore temperature profile, casing/tubing anti-corrosion materials will be selected for the medium and high-temperature zones. Therefore, three experimental conditions were established, as shown in Table 2.

Table 2. Experimental test conditions.

Condition Number	Temperature (°C)	CO ₂ Partial Pressure (MPa)	Floe Velocity	Reaction Cycle	Alloy Steel
1	50	0.30	1.5 m/s	72 h/168 h/336 h	N80, 1 wt.%Cr
2	100	0.63	1.5 m/s	72 h/168 h/336 h	N80, 1 wt.%Cr
3	114	0.73	1.5 m/s	72 h/168 h/336 h	N80, 1 wt.%Cr

The test solution was prepared using 4000 mg/L of Cl⁻ and other analytical grade reagents based on the characteristics of the formation water. The solution was then carefully poured into the reactor, and after the specimens were submerged, the reactor was tightly closed. Nitrogen purging was performed for 10 h to deoxygenate the solution, and then CO₂ was passed through the solution. The reactor contents were then heated and pressurized to the experimental conditions with a flow rate of 1.5 m/s.

2.3. Weight Loss Test

Dynamic corrosion weight loss experiments were carried out for 72, 168, and 336 h. under the experimental temperature and pressure conditions to determine the corrosion rate. After each test, the specimen was thoroughly dried and analyzed for product film composition and pickling. According to ASTM standard G1-03, cleaning involves wiping the surface with a cotton pad soaked in Clark's solution (20 g antimony trioxide + 50 g stannous chloride + 1000 mL 38 wt.% hydrochloric acid). After cleaning, the sample is rinsed with distilled water, followed by ethanol, dried, and then weighed. Mass loss due to corrosion is the difference in mass before exposure and the weight obtained after drying. The corrosion rate is estimated based on mass loss (Δm) using Equation (1) [34]:

$$Vc = \frac{87600\Delta m}{\rho AT} \quad (1)$$

where: Vc is the corrosion rate (mm/a), Δm is the mass loss (g), ρ is the density (g/cm³), A is the exposed area (cm²), and T is the soaking time (h).

2.4. Micro-Structural Analysis

The morphology and elemental composition of corrosion product films were analyzed by TM-3030 desktop scanning electron microscopy (SEM) and QUANTAX-70 energy dispersive spectroscopy (EDS) derived from Hitachi High-Technologies Corporation Tokyo, Japan. The pitting corrosion morphology and depth after pickling was characterized by LSM-900 confocal laser scanning microscopy (CLSM) derived from Carl Zeiss Microscopy GmbH, Jena, Germany.

The pitting corrosion evaluation comprehensively refers to the standard NACE RP0775 and ASTM G46. A quantitative comparison was made using the pitting corrosion rate, metal penetration method, and pitting factor.

2.4.1. Pitting Rate

The depth of the pit was determined by measuring the difference between the depth of the bottom of the pit as viewed under a microscope and the surface of the metal substrate (datum plane). Once the surface pit depth data has been determined, the depth of the deepest pit is divided by the exposure time, using the following Formula (2) [34] to determine the maximum pitting rate.

$$PR(\text{mm/y}) = \frac{\text{depth of deepest pit (mm)} \times 365}{\text{exposure time (days)}} \quad (2)$$

Table 3 gives the qualitative criteria for explaining the measurement of corrosion and pitting rates. The average corrosion and pitting rates shown in Table 3 are compiled from data from the carbon steel system to guide corrosion degree evaluation.

Table 3. Qualitative Categorization of Carbon Steel Corrosion Rates for Oil Production Systems.

Qualitative	Average Corrosion Rate mm/y	Maximum Pitting Rate mm/y
Low	<0.025	<0.13
Moderate	0.025–0.12	0.13–0.20
High	0.13–0.25	0.21–0.38
Severe	>0.25	>0.38

2.4.2. Metal Penetration Method

By measuring the deepest pits, the metal penetration rate is expressed by the average value of the maximum pit depth and the ten deepest pits. In this study, the pitting coefficient

is also used to quantify the degree of metal penetration, which is the ratio of the deepest metal penetration to the average metal penetration determined by the weight loss method. The relationship is as follows Formula (3) [34]:

$$\text{Pitting Factor} = \frac{\text{deepest metal penetration}}{\text{average metal penetration}} \quad (3)$$

When the pitting coefficient is 1, it indicates uniform corrosion; the larger the number, the greater the penetration depth. Since the pitting and uniform corrosion rate in this test environment are not very small, the factor can achieve appropriate quantitative results.

3. Results

3.1. Effect of Experimental Conditions on Corrosion Rate

Figure 2 compares the average corrosion rates of N80 and 1Cr sample specimens after 72, 168, and 336 h exposure to CO₂ corrosion under different temperature and pressure conditions. From this figure, we can see that the average corrosion rate of both materials shows an obvious trend of decrease. Generally, the rate of corrosion of N80 is higher than that of 1Cr, a clear indication that 1Cr can improve the anti-corrosion properties of ordinary carbon steel at medium temperature and low CO₂ partial pressure (50 °C-0.30 MPa) (Figure 2a). However, at 100 °C and 0.63 MPa CO₂ partial pressure, the corrosion rate of 1Cr is approximately 10% and 187% higher than that of N80 (Figure 2b) after 168 h and 336 h, respectively. With further increase in temperature and CO₂ partial pressure (114 °C-CO₂: 0.73 MPa), the corrosion rate of 1Cr remains lower until after 336 h, as we can see an increase of its corrosion rate by 44% than N80 (summarized in Table 7-1*).

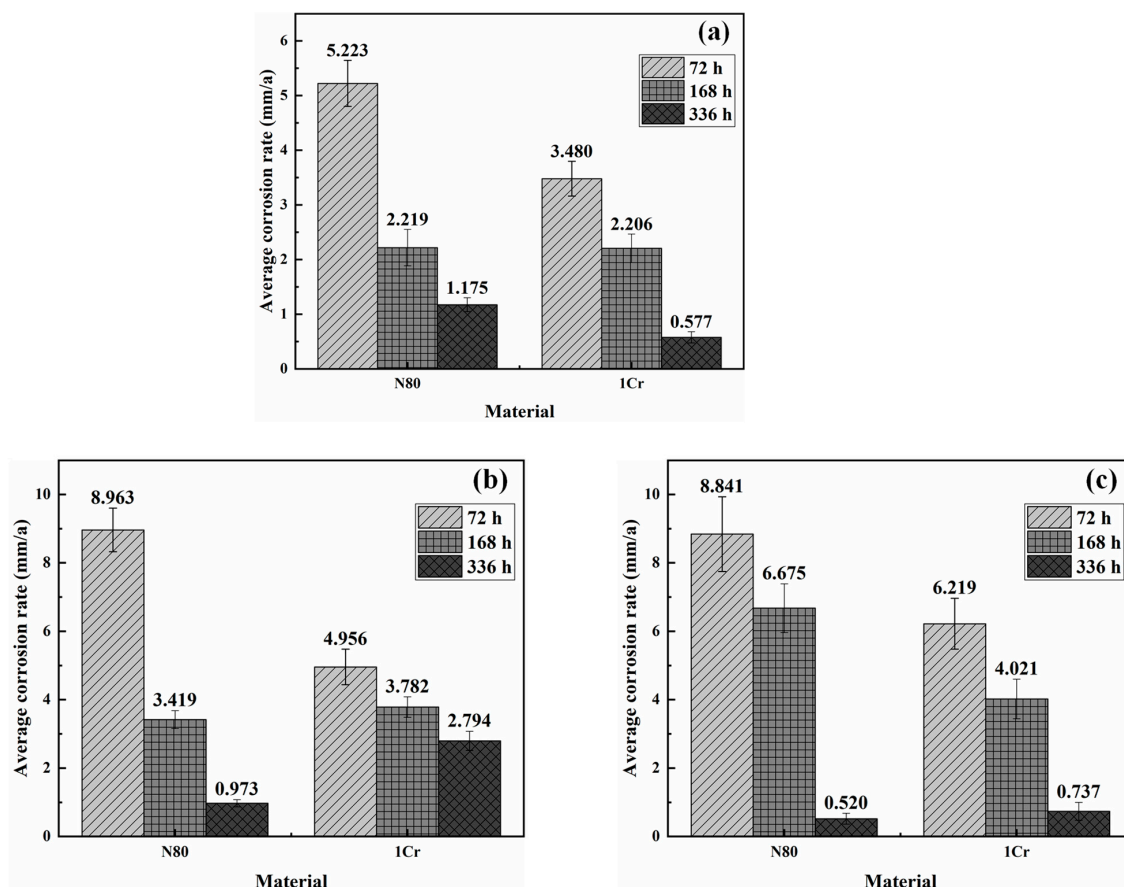


Figure 2. Average corrosion rates of 72 h/168 h/336 h under three corrosion conditions: (a) 50 °C-CO₂: 0.30 MPa, (b) 100 °C-CO₂: 0.63 MPa, (c) 114 °C-CO₂: 0.73 MPa.

The data analysis shows that carbon steel N80 and 1Cr low chromium steel have some corrosion resistance benefits in certain situations. However, according to the qualitative evaluation results of uniform corrosion in Tables 3 and 4, the weight loss corrosion performance of the two low alloy steels in the above three corrosive environments is severe uniform corrosion. Since the above corrosion rate is only a short-term evaluation result, in the actual corrosion conditions, the long-term corrosion rate of the metal matrix will show a significant attenuation law due to the protection of the product film. Therefore, the above corrosion degree only qualitatively reflects the short-term corrosion resistance, and cannot represent the long-term applicability evaluation results.

Table 4. General corrosion rate qualitative of N80 and 1Cr under three corrosion conditions.

Condition Number	Materials	Qualitative/Extent
1	N80	Severe
1	1Cr	Severe
2	N80	Severe
2	1Cr	Severe
3	N80	Severe
3	1Cr	Severe

3.2. Effect of Corrosion Conditions on Product Film

The microscopic corrosion morphology under different experimental conditions of 1Cr steel and N80 steel was analyzed by scanning electron microscope (SEM), as shown in Figure 3. At medium temperature and low partial pressure, a small amount of crystal-like stripes embedded on the dense inner film formed on the surface of N80 steel, as shown in Figure 3a. Energy dispersive X-ray spectroscopy (EDS) analysis of the inner film shows that its main components are Fe, C, and O, as shown in Table 5. The atomic content of O is approximately three times higher than Fe's, so the inner corrosion product is composed mainly of FeCO_3 .

Table 5. EDS analysis of product film of the specimens under different corrosion conditions (normalized mass percentage: less than 0.5% not listed).

Material-Condition	Fe	O	C	Cr
N80-1	46.5	42.7	10.3	/
1Cr-1	44.1	43.9	10.2	1.8
N80-2	48.6	40.2	10.6	/
1Cr-2	50.2	37.6	9.1	2.4
N80-3	46.2	38.7	12.3	/
1Cr-3	45.9	36.1	13.7	2.1

Guo et al. [12,35] proposed that when the degree of saturation of FeCO_3 reaches the critical point, the nucleation rate exceeds the grain growth rate, forming small particle size and even amorphous FeCO_3 film. Additionally, small amount of crystal-like FeCO_3 appear on the surface of 1Cr steel. The exposed product film shows cracking due to air drying, water loss, and increased internal stress (Figure 3b). EDS analysis shows that the elemental composition of the inner film consists of Fe, O, Cr, C, and up to 2.4 wt.% chromium content, which was much higher than the content of steel substrate (1 wt.%). Low chromium steel forms a two-phase mixed membrane of FeCO_3 and Cr(OH)_3 due to competition between the two in a CO_2 corrosion environment. Due to the dissolution of some FeCO_3 in a weakly acidic environment (Formula (4)), the content of Cr(OH)_3 in the product film gradually

increases, improving the toughness, integrity, and compactness of the corrosion film, and presents a fair degree of “chromium-rich” characteristics.

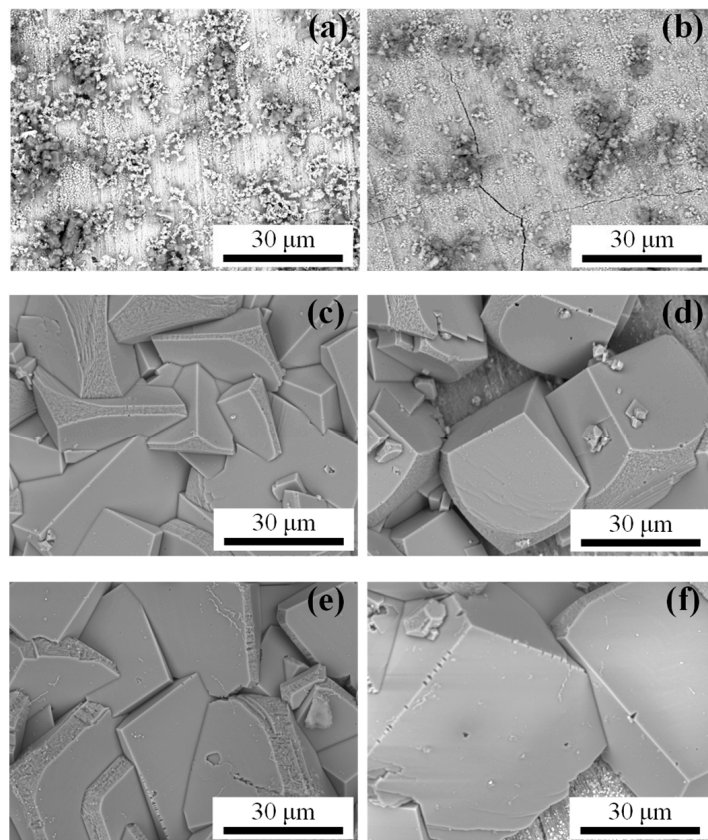
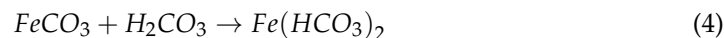


Figure 3. The product film morphology of N80 and 1Cr under three conditions: (a,b) 50 °C-CO₂: 0.30 MPa; (c,d) 100 °C-CO₂: 0.63 MPa; (e,f) 114 °C-CO₂: 0.73 MPa. Note: (a,c,e): N80; (b,d,f): 1Cr.

At high temperatures and high partial pressure, FeCO₃ crystal-like stripes appear on the surfaces of both specimens. Due to flow velocity chipping and scouring effects, some grains have “ring-shaped” edges (Figure 3c–f). However, there is a variance in the thickness and consistency of the corrosion product film (FeCO₃). On the one hand, the outermost layer of N80 is completely covered, compactly stacked, and has no obvious pore characteristics (Figure 4). The results of energy spectrum element analysis showed that the three elements of Fe, O and C were evenly distributed, which confirmed the integrity of the product film and further confirmed that the composition of the product film was ferrous carbonate. On the other hand, the crystal stacking clearance on the outer layer of 1Cr low chromium steel is significantly high, and some secondary layers’ product film is not covered (Figure 5). At the same time, it was found that there was obvious enrichment of Cr element in the exposed sub-outer layer, which confirmed that the main material composition of the amorphous film was Cr(OH)₃. This may be due to the insufficient strength of the corrosion product film generated, which is peeled off the matrix surface due to the shear force generated by the fluid flow. It is also possible that the cation-selective permeability of amorphous Cr(OH)₃ product film prevents the migration of Fe²⁺ ions generated by the anodic dissolution of the metal matrix, leading to the formation of less corrosion products after its deposition occurs on the surfaces. According to the microstructure of Figure 6, it can be inferred that the incompleteness of the 1Cr steel product film is most likely due to the coupling mechanism of the above two effects (summarized in Table 7-2*).

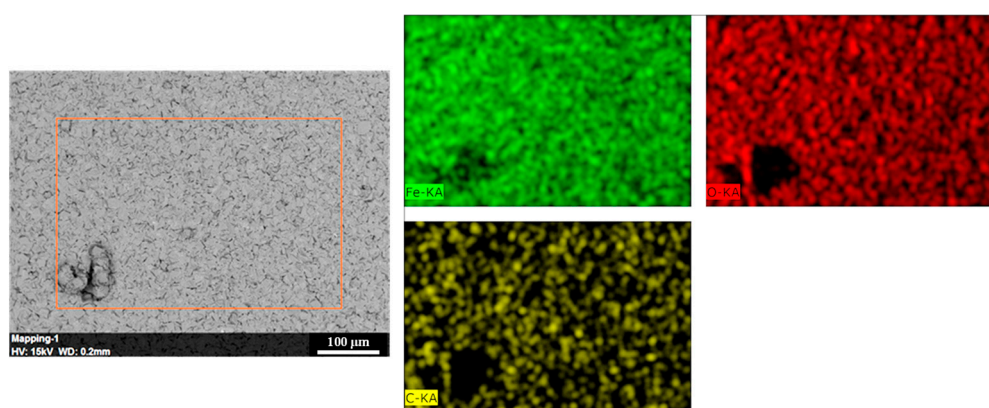


Figure 4. Product film morphology and EDS analysis of N80 Carbon Steel in high temperature and high pressure ($100\text{ }^{\circ}\text{C}$ - CO_2 : 0.63 MPa) corrosion environment.

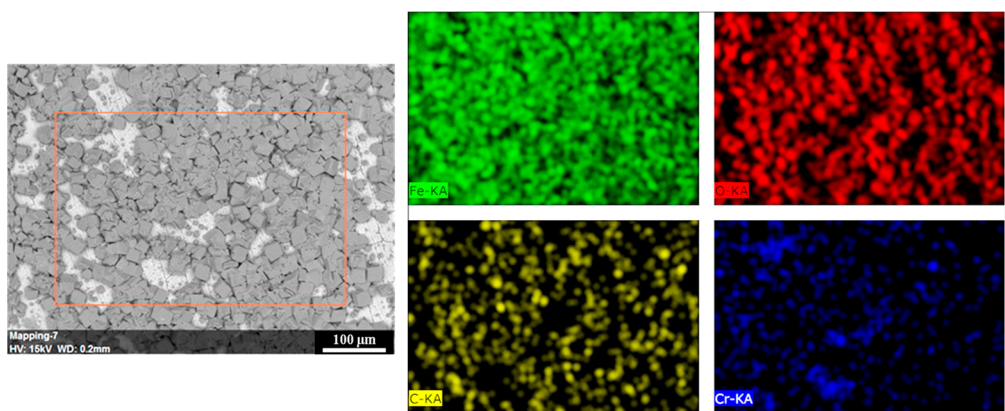


Figure 5. Product film morphology and energy spectrum element analysis of 1Cr steel in high temperature and high pressure ($114\text{ }^{\circ}\text{C}$ - CO_2 : 0.73 MPa) corrosion environment.

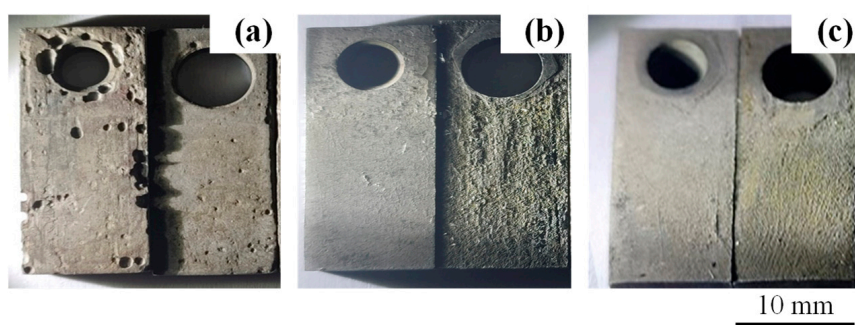


Figure 6. Specimen appearance (N80/1Cr from left to right) under three conditions: (a) $50\text{ }^{\circ}\text{C}$ - CO_2 : 0.30 MPa; (b) $100\text{ }^{\circ}\text{C}$ - CO_2 : 0.63 MPa; (c) $114\text{ }^{\circ}\text{C}$ - CO_2 : 0.73 MPa; after removal of product film.

The observations above indicate that at $50\text{ }^{\circ}\text{C}$ and a CO_2 partial pressure of 0.30 MPa, the crystalline product film on the surface of carbon steel does not inhibit corrosion. Instead, the dense amorphous FeCO_3 film on the inner layer decreases the corrosion rate. The corrosion rate of low chromium steel is primarily controlled by the colloidal mixed product film formed by the co-deposition of FeCO_3 and Cr(OH)_3 . This dense corrosion product film plays a significant role in inhibiting corrosion. At high partial pressure and high temperature, a dense crystalline FeCO_3 film forms on the surface of N80 steel, which blocks the mass transfer process between the metal matrix and the corrosion medium, thus inhibiting further corrosion. However, low chromium steel 1Cr is not immune to corrosion in this environment as its weight loss corrosion rate remains high. Additionally,

its corrosion products are not dense, and the adhesion to the matrix is weak, causing the product film to peel off the matrix surface under fluid shear stress. This results in an incomplete product film on the material surface, and the poor stability of the product film reduces the corrosion resistance of low chromium steel 1Cr at these conditions.

3.3. Effect of Corrosion Conditions on Pitting Characteristics

Figure 6 shows the specimen's appearance after pickling; Figure 7 shows the corresponding pitting pit cross-section shape in ASTM G46 standard; and Figures 8 and 9 are the microscopic corrosion morphology and pit depth measurement. At 50 °C and 0.30 MPa CO₂ partial pressure, we can see both local and pitting corrosion on N80 carbon steel and 1Cr. However, several large "elliptical (Figure 7a)" or "vertical (Figure 7b)" pitting pits are observed on the N80 steel specimen (Figure 8a), with the largest pit having a depth of about 329.04 µm and a width of approximately 712.51 µm (Figure 9a). Nevertheless, the pitting size of 1Cr steel (Figure 9b) is relatively small compared to N80 steel, with a shape of 'Wide, Shallow' (Figure 7c). Its maximum pitting pit depth and width are approximately 131.87 µm and 506.88 µm, respectively.

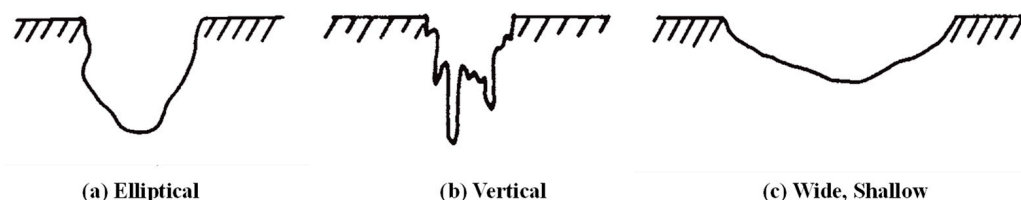


Figure 7. Variations in the cross-sectional shape of pits mentioned in ASTM G46.

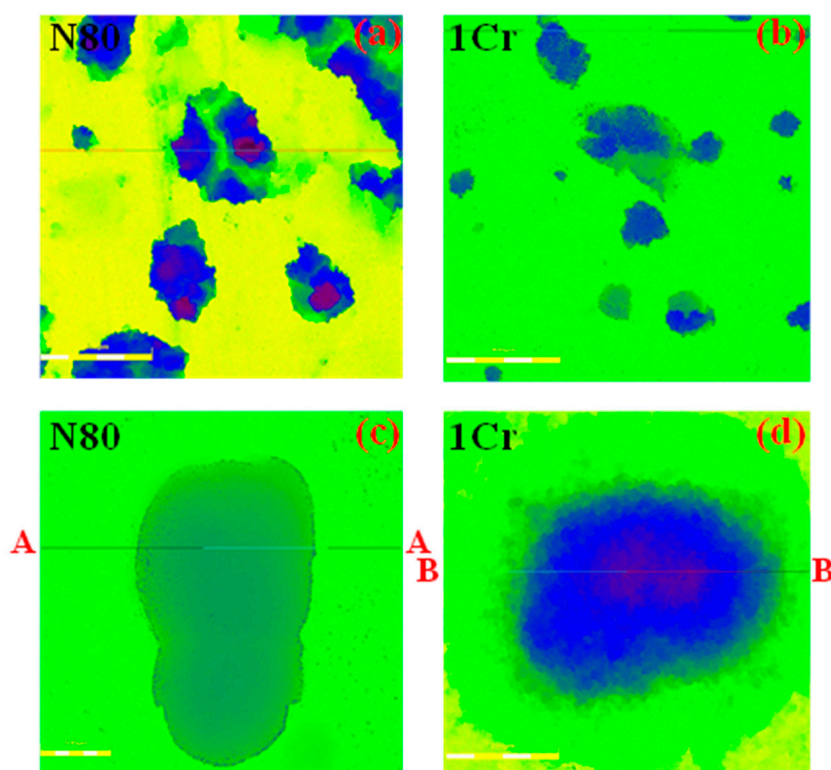


Figure 8. Micrographical analysis of the pitting corrosion at lower temperature-partial pressure (50 °C-CO₂: 0.30 MPa): (a,b): shows pitting density; (c,d) Maximum pit size characterization. Note: A-A/B-B is the cross section at the maximum pitting depth of the pitting pit.

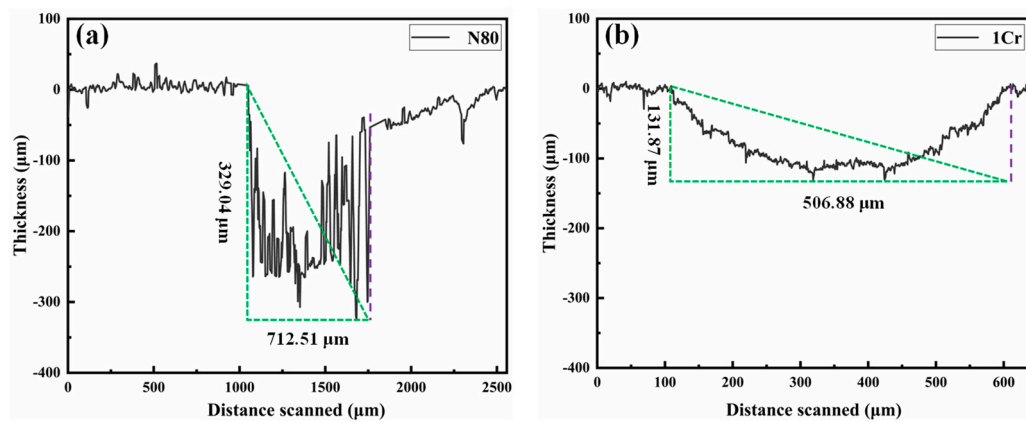


Figure 9. The maximum Pit size measurement and evaluation along the cross-sections: (a) cross-sections A-A (N80); (b) cross-section B-B (1Cr) under the condition of $50\text{ }^{\circ}\text{C}$ - CO_2 : 0.30 MPa.

In addition, the metal penetration depth method quantitatively characterized the pitting corrosion degree. The maximum pitting depth and the average of the ten maximum depths were selected as the quantitative parameters. Figure 10 is the pitting penetration depth and pitting factor characterization evaluation results. The average penetration depth of carbon steel N80 was 301.49 μm, which was significantly higher than that of 1Cr low alloy steel 113.73 μm (Figure 10). In terms of pitting factors, the quantitative results of N80 and 1Cr are 7.30 and 5.96, respectively, showing the rule of $\text{N80} > \text{1Cr} \gg 1$, which further indicates that the corrosion characteristics of the two materials are dominated by pitting corrosion, and the pitting severity of N80 is higher than that of 1Cr steel. The maximum pitting depth was selected to calculate the pitting rate in quantifying the pitting rate. In the same environment, the pitting rate of N80 was 8.579 mm/a, while 1Cr was significantly lower at 3.438 mm/a. Although in the short term, the pitting degree of both materials is classified as severe pitting (Table 6), the pitting condition under long-term service conditions will become relatively mild, so the method is only used to quantitatively and qualitatively compare the advantages and disadvantages of materials. Fundamentally, the pitting density, size, sensitivity and other quantitative parameters of 1Cr low alloy steel are significantly lower than those of N80, indicating 1 wt.% Cr element improves its corrosion resistance.

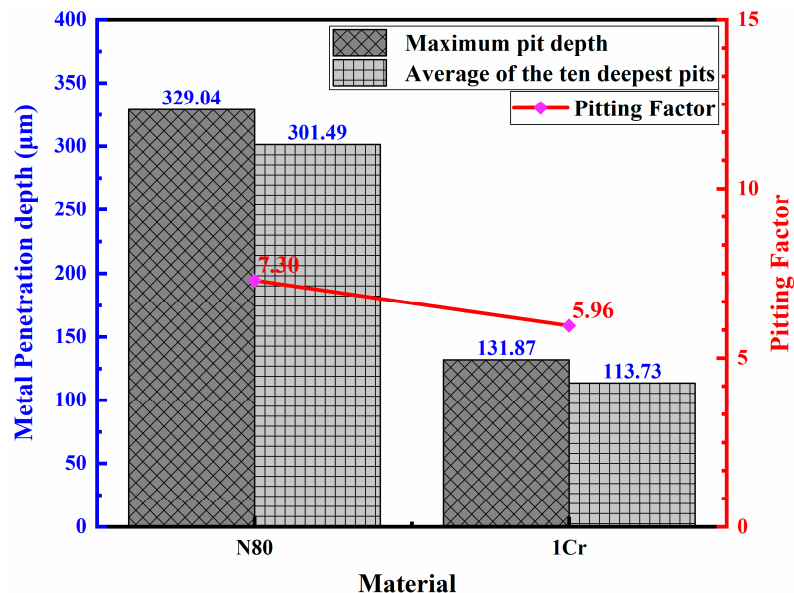


Figure 10. Pitting Penetration Depth and Pitting Factors of N80 and 1Cr at $50\text{ }^{\circ}\text{C}$ - CO_2 : 0.30 MPa.

Table 6. Maximum pitting rate and Qualitative of N80 and 1Cr at 50 °C-CO₂: 0.30 MPa.

Materials	Maximum Pitting Rate (PR)	Qualitative/Extent
N80	8.579 mm/a	Severe
1Cr	3.438 mm/a	Severe

Under the condition of higher temperature and higher partial pressure corrosion, a visual inspection of N80 carbon steel shows a relatively smooth surface, indicating uniform corrosion (Figure 6b,c) (summarized in Table 7-3*). However, macroscopic corrosion morphology investigation, as shown in Figure 11a,c shows a minimal number of deep pitting pits, suggesting that the corrosion products on these pits do not inhibit corrosion. The dissolution of the metal in the corrosion pit produces excess metal cations (Fe^{2+}) so that the Cl^- ions outside migrate inward to maintain electrical equilibrium. Consequently, the acidification autocatalytic reaction caused by accumulating Cl^- ions exacerbates the pitting corrosion.

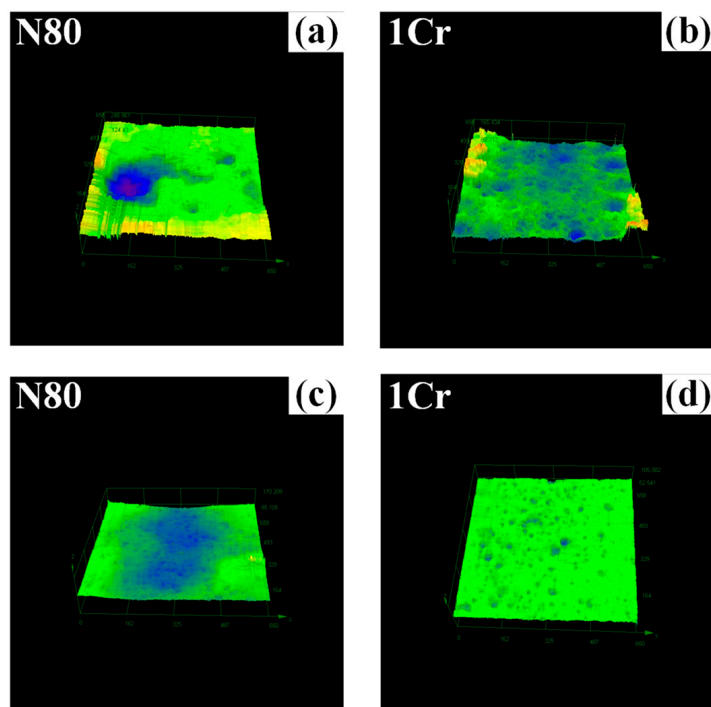


Figure 11. The pitting corrosion density micrographs at high temperature-partial pressure: (a,b): 100 °C-CO₂: 0.63 MPa; (c,d): 114 °C-CO₂: 0.73 MPa.

The corrosion morphology (Figure 6b,c) analysis of 1Cr steel shows that except for a small area at the top of the sample, most of the metal substrate surface is uniformly corroded, resulting in serious thinning and obvious step shape, which is the result of uniform corrosion rate much larger than pitting rate. Combined with the results of micro-point corrosion analysis (Figure 11b,d), it can be seen that the pitting resistance of 1Cr low chromium alloy steel, especially the pitting density, has a certain degree of attenuation compared with N80 carbon steel, and its mesa corrosion can be attributed to the evolution of pitting pits formed in the early stage of corrosion (summarized in Table 7-3*). Due to the enrichment of corrosion product $\text{Cr}(\text{OH})_3$ in the pitting pit, the relative potential in the pitting pit increases, which is higher than the potential in the area around the pit, forming a corrosion environment of large anode and small cathode, promoting the anodic dissolution in the surrounding area, and finally evolving into mesa corrosion.

Table 7. Conclusion Summary.

Number	Results	Conclusions
1*	Effect of experimental conditions on corrosion rate	In certain situations, the corrosion rate of N80 is higher than that of 1Cr, but with the increase in temperature and pressure as well as the passage of time, the corrosion rate of 1Cr is gradually greater than that of N80.
2*	Effect of corrosion conditions on product film	At low temperatures and pressures, the dense amorphous FeCO_3 film on the inner layer of carbon steel reduces the corrosion rate. At high partial pressures and temperatures, the formation of a dense crystalline film of FeCO_3 on the surface of N80 steel inhibits further corrosion, while the low chromium steel 1Cr is not immune to corrosion in this environment.
3*	Effect of corrosion conditions on pitting characteristics	Less pitting at higher temperatures and higher pressures for both N80 and 1Cr. And the pitting resistance of 1Cr low chromium alloy steel, especially the pitting density, has a certain degree of attenuation compared with N80 carbon steel.

4. Discussion

4.1. Mechanistic Insights of Corrosion Resistance Difference

Fe and Cr are relatively active metals, but the activity of Cr is higher than that of Fe. As a result, the anodic reaction of N80 carbon steel with 1 wt.% Cr progresses as expressed in Equations (5) and (6). As the corrosion reaction progresses and ions migrate, reactions expressed by Equations (7) and (8) occur on the metal's surface. When the ionic product (K) of FeCO_3 and Cr(OH)_3 exceeds the solubility product constant (K_{sp}), the solution becomes supersaturated, and a solid film will precipitate on the specimen's surface.



The solubility product constants for FeCO_3 and Cr(OH)_3 corrosion products in aqueous solution are $K_{\text{sp}}(\text{FeCO}_3) = 3.2 \times 10^{-11}$ and $K_{\text{sp}}(\text{Cr(OH)}_3) > 6.3 \times 10^{-31}$, respectively [36]. Therefore, the corrosion product Cr(OH)_3 of 1Cr low chromium steel has better stability. This explains why 1Cr steel has better anti-corrosion properties than N80 carbon steel at medium temperature and low partial pressure. Previous studies in this area [11,19,30,31] report that the corrosion product film of low-chromium steel in a CO_2 environment is composed of a crystalline FeCO_3 outer layer and a continuous, dense, amorphous Cr(OH)_3 inner layer, which retard the anodic reaction (Equation (5)) slowing down the corrosion rate.

However, due to the influence of temperature and acid gas partial pressure, the corrosion reaction mechanism at high temperature and high partial pressure has changed significantly. Figures 12 and 13 are schematic drawings of corrosion mechanism of carbon steel N80 and 1Cr steel under high temperature and pressure respectively. In fact, there are various reasons why the corrosion resistance of N80 is better than that of 1Cr under high temperature and high partial pressure corrosion environment. Primarily, for carbon steel N80, at high temperature, the activation energy E_a of reaction (5)/(7) decreases, and the barrier decreases, resulting in a high concentration of Fe^{2+} ions in the thin liquid layer on

the surface of the metal matrix. Secondly, the higher CO_2 partial pressure not only directly increases the concentration of saturated H_2CO_3 , but also the higher temperature leads to the larger ionization constant K_a and more CO_3^{2-} ions. Under the driving action of the above conditions, the formation rate of the product film on the carbon steel N80 is accelerated, and even the nucleation rate of ferrous carbonate is greater than the growth rate of the crystal nucleus, forming the innermost amorphous film layer, and the corrosion reaction is greatly controlled. In addition, high temperature is beneficial to improve the density of the inner membrane and improve the stability of the membrane components, which further eliminates the risk of localized corrosion, which is consistent with our observations.

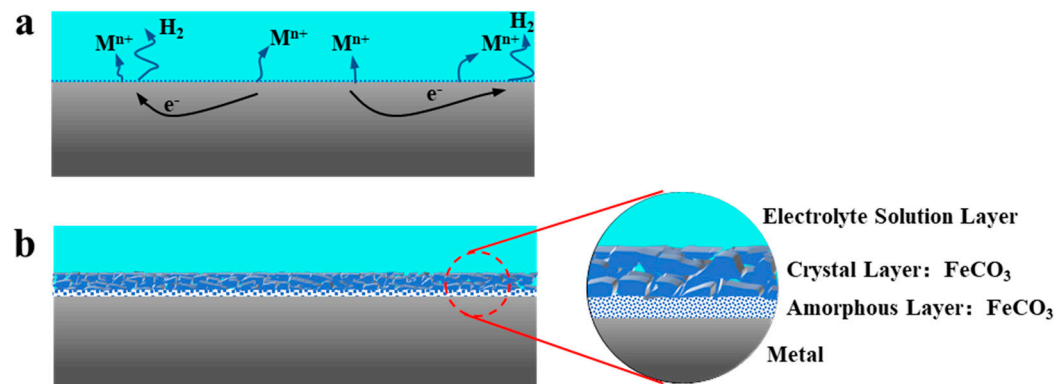


Figure 12. Schematic of Mesa corrosion mechanism of N80 steel under high temperature and high CO_2 partial pressure: (a) Uniform corrosion stage; (b) Corrosion product deposition stage.

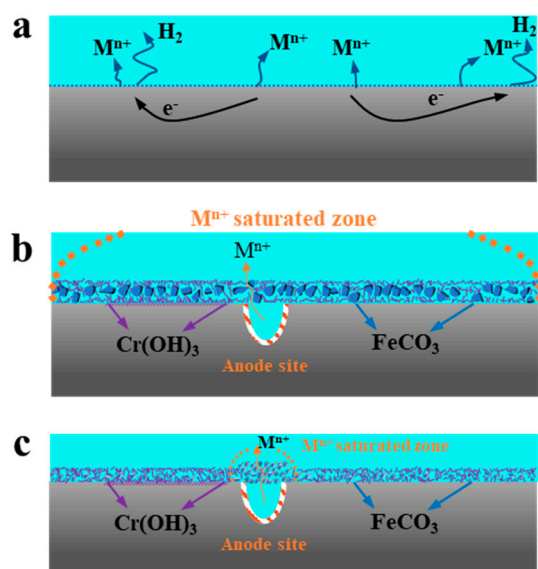


Figure 13. Schematic of Mesa corrosion mechanism of 1Cr steel under high temperature and high CO_2 partial pressure: (a) Uniform corrosion stage; (b) The competitive deposition of corrosion products and pitting incubation stage; (c) Pitting corrosion development and formation stage.

On the contrary, for 1Cr steel, due to the presence of a small amount of Cr element in its composition, amorphous $\text{Cr}(\text{OH})_3$ is formed (Equations (6) and (8)). However, due to the content of Cr element, the coverage of $\text{Cr}(\text{OH})_3$ is greatly restricted, which will lead to the existence of some anode active sites, local corrosion and the formation of dissolution zone. In addition, because $\text{Cr}(\text{OH})_3$ has a certain cation selective permeability, it can effectively prevent anions from passing through the corrosion product film to the metal surface, resulting in a significant decrease in the rate of reaction 7 outside the active corrosion zone. In the anode active area, the initial stage of corrosion is characterized

by the co-precipitation of reaction 7/8, forming the result of competitive deposition of Cr(OH)_3 and FeCO_3 . However, with the progress of the corrosion process, in this acidic environment, the reaction 4 will gradually intensify, making the FeCO_3 in the deposition layer gradually dissolve, resulting in the corrosion products tend to be ‘chromium-rich’. In addition, the presence of Cr(OH)_3 weakens the adhesion between FeCO_3 crystals and the amorphous layer of Cr(OH)_3 , resulting in a decrease in the adhesion of the product film. At the same time, under the influence of continuous fluid shear stress, the loose corrosion product film is easily peeled off. Therefore, based on the above factors, the characteristics of 1Cr tending to local corrosion are formed, which induces the incomplete coverage of FeCO_3 film, and finally leads to the activation corrosion is more serious than that of N80 carbon steel [33,37–39].

4.2. Outlook

The results show that it is incorrect to think that adding 1 wt.% chromium can improve the corrosion resistance of metal materials. The ability of 1Cr steel to resist CO_2 corrosion depends not only on the downhole corrosion conditions, but also on its corrosion characteristics. In further research, the experimental conditions can be refined, and the single variable of temperature and partial pressure can be adopted to more specifically propose the best use conditions of 1Cr steel. In addition, the above evaluation experiments are limited by the test period. Although they can be successfully used to qualitatively compare the corrosion resistance differences and reveal the corrosion mechanism, they cannot truly reflect the corrosion results under long-term corrosion conditions. Therefore, the corrosion behavior under long test cycles can be further studied to more accurately evaluate the applicability of materials. At the same time, the optimal chromium content that can eliminate local corrosion is explored, and combined with electrochemical test methods (such as potentiodynamic plan test and AC impedance spectroscopy), the corrosion reaction kinetics information and interface and product film structure information are more comprehensively revealed.

5. Conclusions

(1) Under high-temperature and high- CO_2 partial pressure conditions, N80 carbon steel has greater corrosion resistance than 1Cr. This is due to its ability to quickly form a corrosion product film that is highly compact and integral, resulting in more prominent local corrosion resistance and lower surface roughness, which expands the application range of carbon steel. However, in practical applications, it may be necessary to increase the wall thickness appropriately to achieve a balance between strength and economy.

(2) Although 1Cr alloy steel develops a ‘chromium-rich’ amorphous secondary outer layer under high-temperature and high-pressure environments, its corrosion resistance is limited by the incomplete outermost dense crystalline FeCO_3 layer, resulting in mesa corrosion and a higher weight loss corrosion rate than N80 carbon steel. Therefore, under such conditions, the 1 wt.% Cr element does not provide corrosion inhibition but exacerbates the risk of localized corrosion due to the uneven amorphous product film.

(3) Under low-temperature and low- CO_2 partial pressure conditions, the corrosion product film of 1Cr alloy steel is enriched with more stable amorphous Cr(OH)_3 due to the difference in solubility product between corrosion products FeCO_3 and Cr(OH)_3 . Meanwhile, the low temperature leads to a slower film-forming speed of FeCO_3 . Therefore, 1Cr alloy steel exhibits more prominent corrosion resistance than carbon steel under these conditions.

(4) The composition and characteristics of the corrosion product film are the main factors controlling the material’s resistance to corrosion. Studying the film formation mechanism under specific corrosion conditions makes it possible to select the appropriate anti-corrosion material.

(5) The above evaluation experiments are limited by the experimental period. Although they can be used to qualitatively compare the differences in corrosion resistance

and reveal the corrosion mechanism, they cannot truly reflect the long-term corrosion results. Therefore, studying the corrosion behavior under long test cycles can provide a more accurate evaluation of the applicability of materials.

Author Contributions: Data curation, M.H. and Z.M.; Methodology, L.W. and G.L.; Project administration, M.H. and W.Y.; Resources, L.Z. and S.Z.; Writing—original draft, J.L., M.L. and Z.M.; Writing—review & editing, Z.M., K.L. and W.Y. All authors have read and agreed to the published version of the manuscript.

Funding: This research was supported by The Project ‘Integrated Design of Corrosion Mechanics and Anticorrosion Material Selection for Injection–production String’.

Institutional Review Board Statement: Not applicable.

Informed Consent Statement: Not applicable.

Data Availability Statement: Data is contained within the article.

Conflicts of Interest: There is no conflict of interest related to this paper.

References

1. Osieczko-Potoczna, K.; Gazda, A.; Dušan, M. Factors determining the construction and location of underground gas storage facilities. *Acta Montan. Slovaca* **2019**, *24*, 234–244.
2. Wang, Y.; Li, J.; Cao, G.Q. Material Optimization of Injection and Production String in Su4 Underground Gas Storage. *Adv. Mater. Res.* **2014**, *962–965*, 448–452. [[CrossRef](#)]
3. Liu, K.; He, N.; Zhang, Y.; Xu, F.; Wang, Y. Safety risk analysis of gas injection and recovery wells in the Xiangguosi Gas Storage and countermeasures. *Nat. Gas Ind.* **2013**, *33*, 131–135.
4. Lei, R.; Zhang, Y.; Zhou, Y.; Chen, Y.; Li, X.; Dong, X. Study on Prediction of Corrosion Rate of Injection and Production Well in Gas Storage. *Saf. Health Environ.* **2017**, *05*, 5–7.
5. Choi, Y.-S.; Young, D.; Nešić, S.; Gray, L.G. Wellbore integrity and corrosion of carbon steel in CO₂ geologic storage environments: A literature review. *Int. J. Greenh. Gas Control* **2013**, *16* (Suppl. S1), S70–S77. [[CrossRef](#)]
6. Xu, L.; Wang, B.; Zhu, J.; Li, W.; Zheng, Z. Effect of Cr content on the corrosion performance of low-Cr alloy steel in a CO₂ environment. *Appl. Surf. Sci.* **2016**, *379*, 39–46. [[CrossRef](#)]
7. Lining, X.U.; Zhu, J.; Wang, B. Influence of Cr Content and pH Value on the SemiPassivation Behavior of Low Cr Pipeline Steels. *Acta Metall. Sin.* **2017**, *53*, 677–683.
8. Chen, L.; Liu, W.; Dong, B.; Zhang, P.; Zhao, Q.; Zhang, T.; Fan, P.; Li, H. Role of Trace Dissolved Oxygen Content in Corrosion Scale of 3Cr Steel in CO₂ Aqueous Environment. *J. Mater. Eng. Perform.* **2022**, *31*, 4864–4876. [[CrossRef](#)]
9. Olsen, S.; Halvorsen, A.M.; Lunde, P.G.; Nyborg, R. CO₂ Corrosion Prediction Model—Basic Principles. In CORROSION 2005; OnePetro: Houston, TX, USA, 2005; p. NACE-05551.
10. Nyborg, R.; Dugstad, A. Understanding and Prediction of Mesa Corrosion Attack. In CORROSION 2003; OnePetro: San Diego, CA, USA, 2003; p. NACE-03642.
11. Chen, C.; Zhao, G.; Yan, M.; Bai, Z.; Yang, Y. Characteristics of CO₂ corrosion scales on 1%Cr-containing N80 steel. *J. Chin. Soc. Corros. Prot.* **2003**, *22*, 338–347.
12. Guo, S.; Xu, L.; Zhang, L.; Chang, W.; Lu, M. Corrosion of alloy steels containing 2% chromium in CO₂ environments. *Corros. Sci.* **2012**, *63*, 246–258. [[CrossRef](#)]
13. Xu, L.; Xie, Y.; Lu, M.; Zhang, L.; Chang, W. Effect Of Temperature On Wet CO₂ Corrosion Of 3%Cr Pipeline Steel. In CORROSION 2012; OnePetro: Salt Lake City, UT, USA, 2012; p. NACE-2012-1348.
14. Guo, S.; Xu, L.; Chang, W.; Zhang, L.; Hu, L.; Lu, M. The Anti-pitting Mechanism of Low Cr Alloy Steel In CO₂ Corrosion Environment. In CORROSION 2012; OnePetro: Salt Lake City, UT, USA, 2012; p. NACE-2012-1357.
15. Qian, J.; Chen, C.; Zheng, S.; Weng, Y. Effect of partial pressure ratio H₂S/CO₂ on mechanical properties of 3Cr oil tube steel. In Proceedings of the 2011 International Conference on Materials for Renewable Energy & Environment, Shanghai, China, 20–22 May 2011.
16. Guo, S.; Xu, L.; Chang, W.; Mi, Y.; Lu, M. Experimental study of CO₂ corrosion of 3cr pipe line steel. *Acta Metall. Sin.* **2011**, *47*, 1067–1074.
17. Bai, Z.Q.; Chen, C.F.; Lu, M.X.; Li, J.B. Analysis of EIS characteristics of CO₂ corrosion of well tube steels with corrosion scales. *Appl. Surf. Sci.* **2006**, *252*, 7578–7584. [[CrossRef](#)]
18. Chen, C.; Minxu, L.U.; Zhao, G.; Bai, Z.; Yan, M. The Eis Analysis of Electrode Reactions of CO₂ Corrosion of N80 Steel. *Acta Met. Sin.* **2002**, *38*, 770–774.
19. Chen, C.; Minxu, L.U.; Zhao, G.; Bai, Z.; Yan, M. Characters of CO₂ corrosion scales on well tube steels N80. *Acta Met. Sin.* **2002**, *38*, 411–416.

20. Ueda, M.; Takabe, H. The Formation Behavior of Corrosion Protective Films of Low Cr Bearing Steels in CO₂ Environments. In *CORROSION 2001*; OnePetro: Houston, TX, USA, 2001; p. NACE-01066.
21. Li, W.; Xu, L.; Qiao, L.; Li, J. Effect of free Cr content on corrosion behavior of 3Cr steels in a CO₂ environment. *Appl. Surf. Sci.* **2017**, *425*, 32–45. [[CrossRef](#)]
22. Chen, C.F.; Lu, M.X.; Sun, D.B.; Zhang, Z.H.; Chang, W. Effect of Chromium on the Pitting Resistance of Oil Tube Steel in a Carbon Dioxide Corrosion System. *Corros. Houst. Tx* **2005**, *61*, 594–601. [[CrossRef](#)]
23. Chen, C.F.; Lu, M.X.; Zhao, G.X.; Bai, Z.Q.; Yang, Y.Q. Effects of temperature, Cl⁻ concentration and Cr on electrode reactions of CO₂ corrosion of N80 steel. *Acta Metall. Sin. Chin. Ed.* **2003**, *39*, 848–854.
24. Chen, C.F.; Lu, M.X.; Zhao, G.X.; Bai, Z.Q.; Yang, Y.Q. The EIS analysis of cathodic reactions during CO₂ corrosion of N80 steel. *Acta Met. Sin.* **2003**, *39*, 94–98.
25. Chen, C.F.; Lu, M.X.; Zhao, G.X.; Bai, Z.Q.; Yang, Y.Q. Mechanical properties of CO₂ corrosion scale on N80 well tube steel. *Acta Met. Sin.* **2003**, *39*, 2219–2224.
26. Chen, C.; Minxu, L.U.; Zhao, G.; Yan, M.; Bai, Z.; Yang, Y. Electrochemical Characteristics of CO₂ Corrosion of Well Tube Steels With Corrosion Scales. *J. Chin. Soc. Corros. Prot.* **2003**, *23*, 139–143.
27. Zhao, G.; Chen, C.; Lu, M.; Li, H. The formation of product scale and mass transfer channels during CO₂ corrosion. *J. Chin. Soc. Corros. Prot.* **2002**, *22*, 363–366.
28. Wu, T.; Wu, H.; Niu, G.; Li, T.; Sun, R.; Gu, Y.; Yuan, R. Effect of Microstructure on the Corrosion Performance of 5% Cr Steel in a CO₂ Environment. *Corrosion* **2018**, *74*, 757–767. [[CrossRef](#)]
29. Wang, C.-L.; Guo, H.-D.; Fang, J.; Yu, S.-X.; Yue, X.-Q.; Hu, Q.-H.; Liu, C.-W.; Zhang, J.-X.; Zhang, R.; Xu, X.-S.; et al. The role of Cr content on the corrosion resistance of carbon steel and low-Cr steels in the CO₂-saturated brine. *Petrol. Sci.* **2022**. ISSN 1995-8226. [[CrossRef](#)]
30. Sun, J.; Yang, L.; Liu, W.; Lu, M. Electrochemical behavior and localized corrosion of X65 steel in high salt concentration brines with CO₂ saturated. *Mater. Res. Express* **2018**, *5*, 026503. [[CrossRef](#)]
31. Sun, J.; Sun, C.; Wang, Y. Electrochemical science effect of cr content on the electrochemical behavior of low- chromium x65 steel in CO₂ environment. *Int. J. Electrochem. Sci.* **2018**, *11*, 8599–8611.
32. Sun, J.; Yapeng, J.; Sun, C.; Jiang, T.; Liu, H. Sulfide Stress Corrosion Cracking Behavior of Low-Cr Steel in H₂S-CO₂ Environment. *Surf. Technol.* **2016**, *45*, 1.
33. Xun, L.; Fang, J.; Wenmei, C. The Carbon Dioxide Corrosion of Tube and Casing in Downhole. *Chem. Eng. Oil Gas* **2006**, *4*, 300–303+250.
34. Protocol, N.S. *Preparation, Installation, Analysis, and Interpretation of Corrosion Coupons in Oilfield Operations*; NACE-SP0775-2013; NACE International: Houston, TX, USA, 2013.
35. Guo, S.; Xu, L.; Zhang, L.; Chang, W.; Lu, M. Characterization of corrosion scale formed on 3Cr steel in CO₂-saturated formation water. *Corros. Sci.* **2016**, *110*, 123–133. [[CrossRef](#)]
36. Dean, J.A. Lange's Handbook of Chemistry. *Mater. Manuf. Process.* **1990**, *5*, 687–688. [[CrossRef](#)]
37. Gu, Y.; Wu, H.-B.; Yuan, R.; Wang, X.-T.; Wu, T.; Shuai, S. Influence of Cr content on corrosion performance of middle Cr alloy steel in CO₂ environment. *Mater. Res. Express* **2019**, *6*, 046511. [[CrossRef](#)]
38. Zhu, J.Y.; Xu, L.N.; Lu, M.X.; Chang, W. Cathodic reaction mechanisms in CO₂ corrosion of low-Cr steels. *Int. J. Miner. Metall. Mater.* **2019**, *26*, 1405–1414. [[CrossRef](#)]
39. Oleksak, R.P.; Tylczak, J.H.; Holcomb, G.R.; Dogan, O.N. High temperature oxidation of steels in CO₂ containing impurities. *Corros. Sci.* **2020**, *164*, 108316. [[CrossRef](#)]

Disclaimer/Publisher's Note: The statements, opinions and data contained in all publications are solely those of the individual author(s) and contributor(s) and not of MDPI and/or the editor(s). MDPI and/or the editor(s) disclaim responsibility for any injury to people or property resulting from any ideas, methods, instructions or products referred to in the content.